

RAL 93052
COPY 2 1261
ACCN 2199 19
RAL-93-052

Science and Engineering Research Council

Rutherford Appleton Laboratory

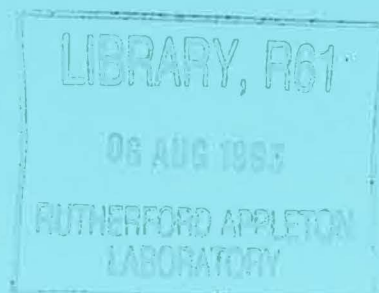
ULP

Chilton DIDCOT Oxon OX11 0QX

RAL-93-052

Neutron Compton Scattering from Amorphous Hydrogenated Carbon

J Mayers T M Burke and R J Newport



July 1993

Science and Engineering Research Council

"The Science and Engineering Research Council does not accept any responsibility for loss or damage arising from the use of information contained in any of its reports or in any communication about its tests or investigations"

NEUTRON COMPTON SCATTERING FROM AMORPHOUS HYDROGENATED CARBON

J. Mayers^a, T. M. Burke^b and R. J. Newport^b

**^a ISIS Neutron Facility, Rutherford Appleton Laboratory, Chilton, Didcot, OX11
0QX,UK.**

^b Physics Laboratory, The University, Canterbury, Kent, CT2 7NR,UK.

PACS 61.12. Ex, 35.80. +s, 61.42.+h

Abstract

Neutron Compton Scattering measurements have been used to determine the kinetic energies of atoms in samples of amorphous hydrogenated carbon (a-C:H), graphite and diamond at momentum transfers between 40 and 300 \AA^{-1} . We find that the kinetic energy of individual carbon atoms is the same within statistical error in a-C:H and graphite but significantly higher in diamond. The kinetic energy of the hydrogen in a-C:H is lower than expected from previous spectroscopic measurements and we infer that the sample contained molecular hydrogen. Observed deviations from the impulse approximation are consistent with theoretical calculations. We discuss future prospects for NCS measurements on non-crystalline materials.

NEUTRON COMPTON SCATTERING FROM AMORPHOUS HYDROGENATED CARBON

1. Introduction

The possibility of measuring nuclear momentum distributions in condensed matter systems by neutron scattering was first suggested by Hohenberg and Platzmann [1] nearly 30 years ago. The method is analogous to the measurement of electron momentum distributions by Compton scattering [2] and measurement of nucleon momenta by Deep Inelastic Scattering [3] and is known as Neutron Compton Scattering (NCS) or Deep Inelastic Neutron Scattering (DINS). The theoretical basis of all three techniques is the impulse approximation (IA), which is exact when the momentum transfer \vec{q} and energy transfer ω are infinite [4,5,6]. When the IA is valid, the scattering cross section is proportional to the distribution of nuclear momentum components along the direction of \vec{q} and can be used to determine $n(\vec{p})$, the distribution of nuclei (and hence atoms) in momentum space.

NCS measurements on strongly bound systems have only become possible since the construction of intense accelerator based neutron sources, which allow accurate inelastic neutron scattering measurements at energy transfers in the eV region [7]. At lower energy transfers the IA is not accurate and $n(\vec{p})$ is not related in a simple way to the observed scattering intensities. In systems with weaker binding lower energy transfers can be used and many early NCS measurements were performed on helium at relatively low energy and momentum transfers, ($\omega < 300$ meV and $q < 15 \text{ \AA}^{-1}$). These studies were motivated primarily by the possibility of directly observing the Bose condensate fraction in superfluid ^4He [8,9,10,11,12,13]. More recently NCS measurements with $15 < q < 40 \text{ \AA}^{-1}$ and incident energies up to 2 eV have been made on condensed phases of helium [14] and neon [15]. There have been a few pioneering studies on various systems at eV energy transfers [16,17,18,19]. The measurements reported here were made on the electron volt spectrometer eVS at ISIS, Rutherford Appleton Laboratory at momentum transfers between 40 and 300 \AA^{-1} and energy transfers between 5 and 20 eV. At such high \vec{q} and ω , $n(\vec{p})$ can be measured even in strongly bound systems. In this paper we present NCS measurements on amorphous hydrogenated carbon (a-C:H), a system of great technological interest. The technique can be applied to determine the kinetic energy of the atoms in any isotropic condensed matter sample (e.g. amorphous and polycrystalline materials, liquids and polymers). In an earlier eVS measurement on aligned polymer chains [20] very good agreement between the measurements and a model based on spectroscopic data was obtained for the hydrogen momentum distribution,

but the instrument count rate was too low for a determination of the momentum of other atoms in the sample. Instrument improvements have allowed a determination of the kinetic energy of both the carbon and the proton in the a-C:H sample studied here.

The technological exploitation of amorphous materials extends back more than two decades and in that period our knowledge of their properties has grown steadily. However the materials at the core of this continuing fundamental and technological interest are relatively complex and a large number of important questions concerning their properties remain unanswered. The continuing generation of new materials opens up the range of questions still further. We address ourselves to the central problem of understanding the relationship between the observed bulk properties of these materials and their structure and binding at the atomic level. In pursuit of this aim we have used a number of different neutron scattering techniques [21,22,23,24] to study the microscopic properties of a-C:H. Amorphous hydrogenated carbon offers one of the broadest ranges of technological potential: a-C:H is also referred to as 'diamond-like' carbon and may be prepared harder, denser and more resistant to chemical attack than any other solid hydrocarbon. These properties, along with optical properties, such as the optical gap and refractive index, may be varied by changing the deposition parameters, which has led to a large number of potential applications.

The structure giving rise to these useful properties is not yet fully understood, with current models involving clusters of sp^2 carbon linked by sp^3 carbon. The reviews of Robertson [25] and Angus et al [26] give a fuller account of these and other models. However the unparalleled real space resolution provided by our recent neutron diffraction data [27] allows us for the first time to comment in detail on carbon bonding environments within the overall random network that makes up this complex material. We see no evidence for the existence of the relatively large sp^2 clusters which lie at the heart of the most commonly used of the current structural models; indeed the data is such that we can state quite clearly that these models must be radically updated.

The role played by hydrogen in determining the properties of a-C:H is crucial to a full understanding of the material. Zou et al [28] have shown that high hydrogen content films (>40 at % hydrogen) are of polymeric nature (high sp^3 content, but soft and with low density) and low-hydrogen content films are of graphitic character (soft films consisting of large clusters of sp^2 carbon). It should be noted however that McKenzie et al²⁹ have produced low-hydrogen content, hard high-density amorphous film. Within the Robertson model, the hydrogen content is seen to stabilise the sp^3 regions reducing the size of any sp^2 clusters, but at the same time increasing the

number of network terminating bonds, leading to a maximum hardness at intermediate hydrogen concentrations.

It is evident that this material possesses an atomic structure of rather greater complexity than of its now much studied analogue a-Si:H. Whilst the short range order in a-C:H (ie the arrangements of its primary σ and π bonds) is of paramount importance in explaining its mechanical/tribological properties, it is order at intermediate distance that is, within the context of these 'heterogeneous' models, likely to account more fully for its electronic and optical properties. Amorphous semiconductors and coatings based on hydrogenated carbon (and silicon:carbon alloys) are of substantial contemporary interest in a technological and in a fundamental sense. We suggest that a full understanding of the structural properties of these amorphous thin film materials at the atomic level is a necessary prerequisite for any coherent understanding of the observed macroscopic properties. Further the ability to control the attributes of these complex systems rests upon the underpinning effect of this understanding. The measurements presented here are a preliminary investigation of the usefulness of NCS for providing microscopic information about the binding and local environment of amorphous materials.

In section 2 we discuss the impulse approximation and describe how the atomic momentum distribution and hence kinetic energy are obtained from eVS data. In section 3 a description of the eVS instrument, sample preparation and experimental details are given. In section 4 we present the results of measurements on samples of a-C:H, graphite and diamond at room temperature. We derive the kinetic energies of the atoms in the samples and analyse the deviations from the impulse approximation which are observed in eVS data. We conclude with a discussion of the implications of the measurements and of future prospects using this new technique.

2. Theory of the NCS technique

2a. The Impulse Approximation

At large enough energy transfer ω and momentum transfer \vec{q} , the dynamic structure factor $S(\vec{q}, \omega)$ is accurately described by the impulse approximation (IA) [30]. The formal statement of the IA for a system containing only particles of mass M is

$$S_M(\vec{q}, \omega) = \int n(\vec{p}) \delta \left[\omega - \frac{(\vec{p} + \vec{q})^2}{2M} + \frac{p^2}{2M} \right] d\vec{p} \quad (1)$$

where $n(\vec{p})d\vec{p}$ is the probability that an atom has momentum in the volume element $d\vec{p}$ centred at \vec{p} . Equation (1) implies that the neutron scatters from a single particle and that the energy transfer is equal to the change in kinetic energy of the target particle. The criteria for the validity of the IA in neutron scattering have been much discussed in the literature [5,6,31]. The physical basis for the IA is that when the energy transfer is much greater than a typical excitation energy of the target system, the time during which the atom and neutron interact is small on the atomic time scale (ie momentum is transferred by an impulsive force - hence the name) and the atom does not have time to move. Thus the potential energy of the struck atom does not change and all the energy transfer is kinetic. If momentum and kinetic energy are conserved, a neutron undergoing momentum loss \vec{q} and energy loss ω must be scattered by an atom with momentum satisfying.

$$\frac{\vec{p} \cdot \vec{q}}{q} = y_M = \frac{M}{q} \left(\omega - \frac{q^2}{2M} \right) \quad (2)$$

Hence from a measurement of the momentum and energy change of the neutron, the component of atomic momentum along the direction of \vec{q} can be measured. For historical reasons [32] the component of momentum along \vec{q} is known as y ; we add the subscript to distinguish between atoms of different mass. It follows from equations 1 and 2 that [5]

$$S_M(q, \omega) = \frac{M}{q} J_M(y_M) \quad (3)$$

where $J_M(y_M)dy_M$ is the probability that an atom has a momentum component parallel to \vec{q} of magnitude between y_M and $y_M + dy_M$. The function $J_M(y_M)$ is known as the 'Compton profile' and due to its physical significance should be symmetric with a maximum at $y_M = 0$. Equations 2 and 3 thus imply that $S_M(\vec{q}, \omega)$ at constant \vec{q} consists of a single peak centred at the 'recoil energy' $\omega_{RM} = q^2/2M$. The corresponding physical interpretation is that a neutron scatters from a stationary atom with an energy transfer ω_{RM} and Doppler broadening due to atomic motion produces a range of energy transfers centred at ω_{RM} . If the system under investigation is isotropic and bound by harmonic forces [33,34,35], $J_M(y_M)$ has the Gaussian form

$$J_M(y_M) = \frac{1}{\sqrt{2\pi\sigma_M^2}} \exp\left(\frac{-y_M^2}{2\sigma_M^2}\right) \quad (5)$$

where σ_M is related to the mean atomic kinetic energy κ_M via

$$\kappa_M = \frac{3\sigma_M^2}{2M} \quad (6)$$

The factor 3 enters because there are three equivalent directions in space for an isotropic system and σ_M is the *rms* momentum component along one of these (arbitrary) directions.

2b. Derivation of Compton Profiles from eVS data

On eVS the energy of the scattered neutron is fixed by a resonance filter difference technique [36]. The final neutron velocity and energy are related by $E_1 = mv_1^2/2$ where m is the neutron mass. The energy of the incident neutron is determined from a measurement of the neutron time of flight (see figure 1) via the equation

$$t - t_0 = \frac{L_0}{v_0} + \frac{L_1}{v_1} \quad (7)$$

where t is the measured time of flight, L_0 and L_1 are the lengths of the incident and the scattered flight paths of the neutron, v_0 and v_1 are the speeds of the incident and scattered neutrons and t_0 is an electronic delay time constant. Then

$$\omega = m(v_0^2 - v_1^2)/2 \quad (8)$$

and

$$q = m(v_1^2 + v_0^2 + 2v_0v_1 \cos \theta)^{1/2} \quad (9)$$

where θ is the scattering angle. From these equations ω and q can be determined for a given time of flight t , if the instrumental parameters t_0, L_0, L_1, θ and E_1 are known and hence the atomic momentum component y_M can be calculated from equation 2. Conversely, a given y_M uniquely specifies a value of t in a time of flight scan. Whether the results are analysed in y_M or t space is a matter of convenience.

The rate at which counts are collected in a time channel of width Δt and centred at time of flight t is³⁷

$$C(t)\Delta t = \left\{ I(E_0) \frac{dE_0}{dt} \Delta t \right\} (\eta(E_1) \Delta \Omega \Delta E_1) \sum_M N_M \frac{d^2 \sigma_M}{d\Omega dE_1} \quad (10)$$

The first expression in parentheses is the intensity of incident neutrons with times of flight between t and $t + \Delta t$. The second factor is the product of the detector efficiency η at energy E_1 ,

the detector solid angle $\Delta\Omega$ and the energy resolution ΔE_1 and is a constant, determined by the instrument geometry and the type of detector. The third factor is the product of N_M , the number of atoms of mass M in the sample and the double differential scattering cross-section for mass M , summed over all atomic masses present in the sample. The double differential scattering cross-section for scattering from mass M is [30]

$$\frac{d^2\sigma_M}{d\Omega dE_1} = b_M^2 \frac{v_1}{v_0} S_M(q, \omega) = b_M^2 \frac{v_1}{v_0} \frac{M}{q} J_M(y_M) \quad (11)$$

where b_M is the scattering length of atoms of mass M and equation 3 has been used. From equations 10 and 11 and taking into account the finite instrument resolution function we obtain,

$$C(t) = \left[\frac{v_1 \eta(E_1) \Delta\Omega \Delta E_1 I(E_0) (dE_0/dt)}{v_0 q} \right] \sum_M N_M b_M^2 M J_M(y_M) \otimes R_M(y_M) \quad (12)$$

where \otimes denotes convolution and $R_M(y_M)$ is the (mass dependent) instrument resolution function in momentum space. The term in parenthesis is a function only of t and is sample independent.

2c. Data Analysis Procedures

The data analysis used in this paper consists essentially of fitting the measured time of flight spectra $C(t)$ to equation 12 with a Gaussian form for $J_M(y_M)$, ie

$$J_M(y_M) = \frac{1}{(2\pi\sigma_M^2)^{1/2}} \exp\left(-\frac{(y_M - \bar{y}_M)^2}{2\sigma_M^2}\right) \quad (13)$$

There are two fitting parameters for each atomic mass, σ_M and \bar{y}_M . All other mass dependent terms in equation 12 can be calculated if the sample composition is known. The value of σ_M obtained determines the atomic kinetic energy for atoms of mass M , while the values of \bar{y}_M can be used to measure deviations from the IA. If the impulse approximation is satisfied, the fits should give $\bar{y}_M = 0$, in agreement with equation 5, and non zero values of \bar{y}_M are therefore evidence for deviations from the IA.

For isotropic samples every scattering angle gives an independent measurement of the Compton profile and the data from different angles can be combined to give a single Compton profile for each atomic mass present (see figures 5 and 8). However the relative separation of peaks from different masses in the time of flight spectra varies with scattering angle (see figure 3), as does the

resolution, and before individual time of flight spectra can be combined, contributions to $C(t)$ other than that from the mass of interest must be subtracted from the data. This is accomplished by the following procedure. The individual time of flight spectra are fitted to equation 12 with the N_M and σ_M for the masses present in the sample used as fitting parameters. Since the impulse approximation is very well satisfied on eVS, the peak positions can be calculated very accurately and are therefore not included as fitting parameters. The fitted peaks other than that corresponding to the mass of interest are subtracted from the time of flight spectra, leaving only the single peak corresponding to mass M. This single time of flight peak is converted to a Compton profile in momentum space by use of equations 2 and 7 to 10. A weighted mean of the spectra from individual detectors gives the final data set $J_M^a(y_M)$

$$J_M^a(y_M) = \left[\sum_{\theta} A_M^{\theta} R_M^{\theta}(y_M) \right] \otimes J_M(y_M) = R_M(y_M) \otimes J_M(y_M) \quad (14)$$

The distribution $J_M^a(y_M)$ is the true Compton profile, $J_M(y_M)$, convoluted with a mean resolution function for mass M, $R_M(y_M)$, which is a sum of the resolution functions at the different scattering angles, weighted by the factors A_M^{θ} . The factor A_M^{θ} is proportional to the detected intensity at the scattering angle θ and depends upon the instrument geometry, detector efficiency and the angular distribution of scattered intensity. The composite resolution function $R_M(y_M)$ can be determined precisely from calibration measurements [38].

It has been shown by Sears [5] that most of the error introduced into the measured value of σ_M by deviations from the impulse approximation can be eliminated by symmetrisation of the data about $\bar{y}_M = 0$. This procedure has been followed in the analysis of the data presented here and typically increases the atomic kinetic energy κ derived from the uncorrected measurements by $\sim 4\%$. This should be compared with statistical accuracies of $\sim 1\%$ which were obtained for the hydrogen kinetic energy and $\sim 4\%$ for the carbon kinetic energy in 24 hours counting time with the current detector system on eVS. At present the symmetrisation procedure should be adequate to reduce FSE to a level comparable with the statistical accuracy of the measurement, but more sophisticated correction procedures will be necessary for future measurements undertaken with higher statistical accuracy.

3. Experimental

3a. The eVS instrument

The eVS spectrometer is illustrated in figure 2 and is described in more detail elsewhere [38,39]. There are 2 banks of 10 ^3He detectors placed symmetrically on either side of the beam line at scattering angles between 35° and 55° and a further 2 symmetrical banks, each of 15 ^3He detectors at scattering angles between 140° and 150° . The forward banks are used mainly for studies of hydrogen, as the hydrogen scattering cross section is strongly anisotropic at eV incident energies, with virtually no backscattering. This restriction is a kinematic consequence of the closeness of the mass of the neutron and the hydrogen atom and does not apply to heavier atoms. Since the instrument resolution improves with increasing scattering angle [40] the backscattering detectors are preferred for measurements on heavier masses. A resonance foil difference technique is used to define the energy of the scattered neutron [36]. At forward angles a gold foil is used to fix the scattered energy at 4922 meV, while at backscattering a uranium foil gives three independent useful measurements at final energies of 6671, 20872 and 36680 meV.

The resolution function $R_M^\theta(y_M)$ for a detector in a particular bank and using a particular analyser resonance is determined by the uncertainties in the measured values of the time of flight t and the distribution of L_0 , L_1 , θ and E_1 values allowed by the instrumental geometry and analyser foil resolution. Uncertainties in L_0 arise primarily from the finite depth of the neutron moderator [38] those in L_1 and θ from the finite sample and detector sizes and those in t from jitter in the detector electronics. All resolution contributions except for the resolution function of the gold foil are well described by Gaussians; the gold foil energy resolution is described by a Lorentzian shape. The widths of the different resolution components and the corresponding resolution components in momentum space are given in tables 1 and 2. The resolution of the hydrogen measurement varies strongly with scattering angle and values in momentum space are given for the detectors at the maximum and minimum scattering angles. The resolution in the carbon measurements varies by less than 3% over the bank of backscattering detectors and the standard deviation of the resolution component is given for the detector at the centre of the bank, for each uranium resonance used. The resolution of the hydrogen measurement in momentum space is dominated by the energy resolution component, but for carbon the dominant contribution is the time jitter in the detector electronics particularly for measurements using the two higher energy uranium resonances.

3b. Experimental Details

The a-C:H sample was prepared using a saddle-field fast-atom (ie neutral particle) source [41] with acetylene as the precursor gas; the deposition parameters pertain to the hard form of the sample (-an effective beam energy of 960 eV and operating at 1.4×10^{-4} mbar system pressure). Knoop hardnesses of 2000 H_K have been measured [42] for this material (c.f. 6000-11000 H_K for diamond [26]), although hardnesses greater than 6000 H_K have also been observed. The macroscopic sample density was determined as 1.8 gm.cm^{-3} using a residual volume technique, and the hydrogen content was determined at 35 at % using a Carlo-Erba CHN combustion analyser. The samples were run at room temperature and suspended in the beam inside an aluminium foil container. The scattering geometry was plane slab with the slab perpendicular to the beam and with a small sample thickness to reduce multiple scattering effects. The scattering from the a-C:H sample was strongly anisotropic due to its hydrogen content, scattering 6% of the beam at 45° , but only 1% at 145° . The graphite sample was a 4% scatterer while the diamond scattered 6% of the incident beam. The aluminium sample container scattered $\sim 0.2\%$ of the incident beam.

4. Results

4a. Atomic Kinetic Energies

Neutron time of flight spectra collected from a-C:H at the ten different angles available in the forward scattering banks are shown in figure 3. The left hand peak is produced by scattering from hydrogen and is well separated from other sources of scattering particularly at large scattering angles. The individual time of flight spectra were fitted to equations 12 and 13 and the fitted peaks corresponding to the carbon and aluminium scattering were subtracted from the data as described in Section 2c. The time of flight spectra were converted to \bar{y}_M and the mean Compton profile for hydrogen in a-C:H, (equation 14) was calculated. The result is shown in figure 4. The solid line is a fit with a $J_M(y_M)$ of the form given by equation 13 and with \bar{y}_M and σ_M as fit parameters. The dotted line is the instrument resolution function, ie $R_M(y_M)$ of equation 14. The values of \bar{y}_M and σ_M obtained from the fit are given in Table 3. After symmetrising about $y_M = 0$ and repeating the fit we obtain a slightly higher value (σ_{MS}) for the standard deviation. The kinetic energy of the hydrogen can be calculated from equation 6. With σ in \AA^{-1} and κ in meV, $\kappa = 6.2705 \sigma^2 / M$ and we obtain the values of kinetic energy given in the second row of Table 3

As a check on the consistency of the data, the atomic kinetic energies were derived by a second procedure. The spectra were fitted individually using the same form for $J_M(y_M)$, but the resolution function $R_M^\theta(y_M)$ appropriate to the different scattering angles. The values of both σ_M^θ and σ_{MS}^θ obtained from fits to the different spectra are shown as a function of scattering angle in figure 5. The fact that there is no systematic variation with scattering angle, despite a factor two variation in resolution, suggests that any errors in the resolution function have negligible effect on the value of the kinetic energy derived from the data. It also suggests that deviations from the impulse approximation are small. The mean of the values obtained from the unsymmetrised ($\bar{\sigma}_M^\theta$) and symmetrised ($\bar{\sigma}_{MS}^\theta$) data are also given in table 3. The excellent agreement of both the values and the statistical errors of the kinetic energies deduced by the two methods of data analysis shows that systematic errors are small.

The momentum distribution of the C atoms in a-C:H, graphite and diamond was derived from the backscattering detectors by an analogous procedure. The sum of the 30 time of flight spectra from the backscattering detectors is shown in Figure 6 for the a-C:H sample. The three distinct peaks correspond to the three uranium resonances at 6671, 20872 and 36680 meV, each of which gives a separate measurement at momentum transfers of ~ 110 , 200 and 270 \AA^{-1} respectively. The expected positions of the C and Al peaks are indicated. Hydrogen scattering is negligible at backscattering angles, as previously mentioned. After subtraction of the small Al contribution and conversion to momentum space, the 6671 U resonance gives the mean Compton profile for carbon in diamond shown in figure 7. The same procedures of fitting and symmetrisation used for analysis of the H atom data were followed for the C atom data for each of the three resonance energies in each sample. The results are given in Tables 4, 5 and 6 for a-C-H, graphite and diamond respectively.

It can be seen from Tables 3 to 6 that values of the values of $\bar{\sigma}_{MS}^\theta$ and σ_{MS} are consistent within statistical error except for the a-C:H results. It seems most likely that this is due to the poor statistical accuracy of the data in individual time of flight spectra collected from a-C:H and consequent instabilities in the fitting procedures. This suggests that the σ_{MS} values provide the most reliable guide to the atomic kinetic energies, as they were derived from a fit to the mean spectrum, which has much better statistical accuracy than spectra from individual detectors. This supposition is supported by the fact that the consistency of the values of σ_{MS} obtained from the different resonance energies is much better than for $\bar{\sigma}_{MS}^\theta$. The symmetrisation of the data increases the derived value of the kinetic energy by $\sim 2\%$ in both hydrogen and carbon (and for the reasons mentioned at the end of section 2c the symmetrised values σ_{MS} should be more

accurate). The σ_{MS} values are collated in table 7, together with the corresponding kinetic energies of the atoms in the three samples.

4b. Final State Effects

There have been many theoretical papers on the form and size of FSE [31], but very little published experimental data. It is thus worthwhile to examine the deviations from the impulse approximation which are present in the data. Typical deviations from the IA take the form which can be observed in Figure 4, with a shift of the peak maximum from the origin of momentum space to negative values. The value $\bar{y}_M = -0.34 \pm 0.02$ obtained from the fit to figure 4 is $\sim 7\%$ of the value of σ_{MS} , in agreement with predictions [35] that deviations from the IA should be $\sim \sigma_{MS}/q$; at the mean momentum transfer of 50 \AA^{-1} corresponding to a scattering angle of 45° , $\sigma_{MS}/q \sim 8\%$. The carbon data also gives shifts in agreement with this rough estimate with typical shifts of $\sim 1 \text{ \AA}^{-1}$ compared with widths of $\sim 14 \text{ \AA}^{-1}$ at momentum transfers of $\sim 200 \text{ \AA}^{-1}$, ie a 7% shift with a σ_{MS}/q of 7%.

From a fit of the form given by equation 12 to an individual time of flight spectrum, values of \bar{y}_M^0 can be obtained for each atomic mass and each scattering angle. If the impulse approximation is satisfied then the fits should give $\bar{y}_M^0 = 0$ at all scattering angles and for all masses. In practice small shifts to negative values of \bar{y}_M^0 of the type shown in Figure 5 for the mean spectrum are obtained. In the fits to individual spectra, the value \bar{y}_M^0 obtained from a fit corresponds to a particular point in a time of flight scan and hence specifies unique values of energy and momentum transfer, which we denote as \bar{q}_M and $\bar{\omega}_M$. If the impulse approximation is satisfied and $\bar{y}_M^0 = 0$, \bar{q}_M and $\bar{\omega}_M$ should be linked via $\bar{\omega}_M = \bar{q}_M^2 / 2M$. In Figure 8 we show experimental values of $\bar{\omega}_M$ as a function of \bar{q}_M^2 for the hydrogen peak. The solid line is a straight line fit to

$$\bar{\omega}_M = \frac{\bar{q}_M^2}{2\alpha} \quad (15)$$

with α as an adjustable parameter. The value of α obtained from the fit is given in table 8. It can be seen that α is $0.6 \pm 0.2\%$ higher than the free proton mass of 1.0073 amu. It is clear that the impulse approximation is very well satisfied by the data, but that deviations from the IA are statistically significant.

Theoretical work [6,43] has suggested that $\bar{\omega}_M$ should be less than $\bar{q}_M^2 / 2M$ by an amount which is approximately equal to the atomic kinetic energy and independent of the magnitude of \bar{q}_M . In

figure 9 we show the quantity $\varepsilon = \bar{\omega}_M - \bar{q}_M^2 / 2M$ as a function of \bar{q}_M^2 for hydrogen. The mean value of ε , given in table 8 is 54 ± 6 meV which is 37% of the kinetic energy of $\kappa=144.5$ meV derived from the width of the peak (Table 8). Although the theory is in semiquantitative agreement with experiment, Figure 9 suggests that ε increases with q and is not strictly a constant.

Figure 10 shows the values of $\bar{\omega}_M$ obtained as a function \bar{q}_M^2 for the carbon atom in a-C-H, together with a fit to equation 14. The three resonances produce three clusters of 30 points. Values of α and ε for the carbon atoms in the three samples were obtained by an identical procedure to that described above for the hydrogen atoms in a-C-H and are also given in Table 8. α is again consistently greater than the free atomic mass of 12.01 and the parameter ε is negative, with a value which is between 25 and 50% of the kinetic energy.

The broad agreement between theory and experiment suggests both that the theory is well founded and that the data is accurate. Thus methods of data correction, such as the symmetrisation procedure used in the previous section, should remove the 2-5% error in the observed momentum distributions which are caused by inaccuracies in the IA at the finite q of the measurement.

5. Conclusions

At the current level of statistical accuracy no significant difference can be detected between the kinetic energy $\kappa_c=103.9 \pm 4.4$ meV of C in a-C:H and the value of 108.3 ± 3.0 meV obtained in graphite, but the kinetic energy of C in diamond is significantly larger at 120.7 ± 3.2 meV. This agrees with the conclusion from diffraction and neutron spectroscopy [21,44] that the dominant carbon site in a-C:H is sp^2 -like, although it is evident from the diffraction data that the sp^2 sites are almost entirely olefinic in character, with little aromatic/graphitic bonding. We note that the measured kinetic energy in graphite agrees very well with previous measurements of Paoli et al [18] who obtained a value of 105 ± 5 meV. For both graphite and diamond the measured kinetic energies are significantly higher than the predictions of calculations based on the density of vibrational states. In graphite a calculation based on a calculated density of states [18,45] gave a kinetic energy of 92 meV, 15% lower than the measured value. In diamond a calculation in the Debye model, with a Debye temperature of 1860K predicts a kinetic energy of 90 meV, 25% lower than the measured value. The calculations assume that the C-C interaction potential is harmonic and the higher values of the carbon kinetic energy which we measure suggests that

anharmonic terms in the potential are important. This is perhaps not surprising given the light mass and strong binding of carbon atoms, which produce a large zero point energy. Our measurements are consistent with other measurements on light atoms [46] which also give kinetic energies somewhat larger than calculations based on a harmonic model.

The measured kinetic energy of the hydrogen atom $\kappa_H=145.7\pm 0.9$ meV contains two essentially independent components. The first is the energy due to the C-H vibration in a reference frame where the carbon atom is stationary and the second comes from the motion of the carbon atom to which the hydrogen is attached. The latter contributes an energy $\sim M_H \kappa_C / M_C = 8.7$ meV, where M_H and M_C are the masses of the hydrogen and carbon atoms. Thus the kinetic energy associated with the C-H bond is 137 meV. Previous measurements [21] assigned a stretch mode of energy $\omega_s=362$ meV and various modes of vibration perpendicular to the bond axis with vibrational energies in the range $\omega_b=130-185$ meV. At room temperature the hydrogen atom is essentially in the vibrational ground state and each vibrational mode of energy ω contributes a kinetic energy of $\omega/4$. The kinetic energy of the proton in the bond is thus

$$\kappa = \frac{1}{4}(\omega_s + 2\omega_b) \quad (15)$$

The values for ω_b and ω_s given above predict a kinetic energy of between 156 and 183 meV, depending upon the value taken for ω_b , if it is assumed that all H atoms are in C-H bonds. This is significantly greater than the measured value and suggests that not all H atoms are bound to carbon atoms. Neutron spectroscopy on the same sample indicated that molecular hydrogen was present in the sample, though quantitative measurements were not possible [21]. If it is assumed that the discrepancy between the measured and expected kinetic energies of the hydrogen is entirely due to the presence of molecular hydrogen, the fraction η of molecular hydrogen in the sample can be calculated. The kinetic energy of H in H₂ is 64.6 meV and $\omega_b=130$ meV gives $\eta=0.21$, while $\omega_b=185$ meV gives $\eta=0.40$. These are surprisingly large values given the weakness of the associated features in diffraction data and inelastic neutron scattering measurements.

This first published measurement on an amorphous material using the NCS technique gives an indication of the information which can be obtained about structure and binding. Recent measurements on molecular hydrogen [47] have shown that the peak shape of $J(y)$ can be used to determine the form of the proton wavefunction even in isotropic systems. With better statistical accuracy and resolution it will be possible to measure anisotropies in the local binding potential of atoms in amorphous and other non-crystalline materials. More accurate data on the q dependence

of final state effects also offers the possibility of using the recoiling atom as a probe of the local environment, in a way which is analogous to EXAFS. The technique would be most sensitive to the environment around atoms of low mass, where EXAFS fails. Orders of magnitude increases in the sensitivity of NCS measurements can be relatively easily obtained by improvements in count rate and resolution and future measurements will provide much more precise and detailed information about the dynamics and structure of non-crystalline materials.

Acknowledgements

We are grateful for the help of Dr. J. Franks and Dr. P. Revell, who prepared the high quality a-C:H samples. One of us (TMB) acknowledges the support of an SERC/CASE studentship.

TABLES

Table 1.

The resolution widths are the Lorentzian HWHM for E_1 and the Gaussian standard deviation for other parameters. The third and fourth rows contain the instrument resolution components in momentum space for hydrogen at scattering angles of 35° and 55° respectively.

	L_0	L_1	θ	t	E_1
Parameter Value	11.055±0.01 m	0.875±0.005 m	45±0.2°	-6.4 ±0.2μsec	4922±10 meV
Resolution Width	0.02±0.05 m	0.009±0.001 m	0.58±0.02°	1.45±0.05μsec	139±4 meV
y resolution at 35°	0.125 Å ⁻¹	0.07 Å ⁻¹	0.49 Å ⁻¹	0.34 Å ⁻¹	1.08 Å ⁻¹
y resolution at 55°	0.06 Å ⁻¹	0.05 Å ⁻¹	0.49 Å ⁻¹	0.24 Å ⁻¹	0.57 Å ⁻¹

Table 2.

The different components of the resolution width in atomic momentum space (denoted by Δy) are calculated for $M = 12$ (carbon) and for the different detection energies provided by the Uranium foil resonances. The energy and resolution widths for the lowest energy U resonance are given. The corresponding values for the other two U resonances used are 20872 meV with a resolution width of 140±20 meV and 36680 meV with a resolution width of 240±30 meV. All resolution widths are Gaussian standard deviations. Resolutions in momentum space are calculated for the detector at the centre of the bank, ie for a scattering angle of 145° . The standard deviation of the total Gaussian resolution function in momentum space is given in the last column.

	L_0	L_1	θ	t	E_1	Total
Parameter Value	11.055±0.005m	1.0±0.005 m	145±0.1°	-5.6±0.2μsec	6671±1meV	
Resolution Width	0.02±0.005 m	0.009±0.002m	0.51±0.02°	1.45±0.05μsec	60±4 meV	
Δy ($E_1=6671$ meV)	0.69 Å ⁻¹	0.36 Å ⁻¹	0.16 Å ⁻¹	2.07 Å ⁻¹	1.89 Å ⁻¹	2.9 Å ⁻¹
Δy ($E_1=20872$ meV)	1.2 Å ⁻¹	0.64 Å ⁻¹	0.28 Å ⁻¹	6.4 Å ⁻¹	2.3 Å ⁻¹	6.9 Å ⁻¹
Δy ($E_1=36680$ meV)	1.6 Å ⁻¹	0.84 Å ⁻¹	0.37 Å ⁻¹	11.2 Å ⁻¹	3.1 Å ⁻¹	11.8 Å ⁻¹

Table 3

Standard deviations of the (assumed) Gaussian Compton profile for H in a-C:H and associated kinetic energies, derived by the fitting procedures described in the text. The errors are the statistical errors derived from the fits. Values with superscript θ are the mean of values derived from fits to individual detectors. Values without superscripts were derived from a single fit to the mean Compton profiles defined by equation 14.

	$\bar{\sigma}_M^\theta$	$\bar{\sigma}_{MS}^\theta$	σ_M	σ_{MS}	\bar{y}_M
Values in \AA^{-1}	4.73 ± 0.02	4.82 ± 0.015	4.75 ± 0.02	4.84 ± 0.015	-0.34 ± 0.02
Kinetic Energies (meV)	139.2 ± 1.1	144.5 ± 1.2	140.3 ± 1.1	145.7 ± 0.9	

Table 4 Results of analysis for C in a-C-H

Resonance Energy	$\bar{\sigma}_M^\theta \text{ \AA}^{-1}$	$\bar{\sigma}_{MS}^\theta \text{ \AA}^{-1}$	$\sigma_M \text{ \AA}^{-1}$	$\sigma_{MS} \text{ \AA}^{-1}$	\bar{y}_M
$E_1=6671 \text{ meV}$	12.4 ± 0.7	13.0 ± 0.4	13.8 ± 0.5	14.0 ± 0.3	-1.2 ± 0.4
$E_1=20872 \text{ meV}$	8.9 ± 1.4	10.7 ± 0.8	13.5 ± 0.9	13.8 ± 0.6	-1.9 ± 0.7
$E_1=36680 \text{ meV}$	11.2 ± 2.8	14.3 ± 1.7	15.1 ± 1.6	15.8 ± 1.0	-2.1 ± 1.3
Mean values.	11.7 ± 0.6	12.9 ± 0.4	13.8 ± 0.5	14.1 ± 0.3	

Table 5 Results of analysis for C in graphite

Resonance Energy	$\bar{\sigma}_M^\theta \text{ \AA}^{-1}$	$\bar{\sigma}_{MS}^\theta \text{ \AA}^{-1}$	$\sigma_M \text{ \AA}^{-1}$	$\sigma_{MS} \text{ \AA}^{-1}$	\bar{y}_M
$E_1=6671 \text{ meV}$	13.5 ± 0.3	13.7 ± 0.2	14.1 ± 0.3	14.2 ± 0.2	-0.3 ± 0.2
$E_1=20872 \text{ meV}$	13.8 ± 0.7	14.2 ± 0.2	15.2 ± 0.5	15.3 ± 0.4	-0.4 ± 0.4
$E_1=36680 \text{ meV}$	9.8 ± 1.0	11.6 ± 0.5	13.8 ± 0.7	14.0 ± 0.5	-1.4 ± 0.6
Mean values	13.3 ± 0.3	13.8 ± 0.3	14.3 ± 0.2	14.4 ± 0.2	

Table 6 Results of analysis for C in diamond

Resonance Energy	$\bar{\sigma}_M^0 \text{ \AA}^{-1}$	$\bar{\sigma}_{MS}^0 \text{ \AA}^{-1}$	$\sigma_M \text{ \AA}^{-1}$	$\sigma_{MS} \text{ \AA}^{-1}$	\bar{y}_M
$E_1=6671 \text{ meV}$	14.7±0.3	14.9±0.2	14.9±0.2	15.1±0.2	-0.9±0.2
$E_2=20872 \text{ meV}$	14.5±0.5	14.7±0.3	15.4±0.4	15.5±0.3	-0.9±0.4
$E_3=36680 \text{ meV}$	13.2±0.7	13.8±0.5	14.6±0.7	14.7±0.5	-1.0±0.6
Mean values	14.5± 0.2	14.7± 0.2	15.0± 0.2	15.2± 0.2	

Table 7 Mean kinetic energies of atoms

Atom	$\sigma_{MS} \text{ \AA}^{-1}$	Kinetic energy (κ) in meV
H in a-C:H	4.84±0.015	145.7±0.9
C in a-C:H	14.1±0.3	103.9±4.4
C in graphite	14.4±0.2	108.3±3.0
C in diamond	15.2±0.2	120.7±3.2

Table 8 Parameters derived from fits to peak positions

	α	ϵ
H	1.013 ± 0.002 amu	-54 ± 6 meV
C (a-C:H)	12.03 ± 0.05 amu	-50 ± 18 meV
C (GRAPHITE)	12.04 ± 0.03 amu	-27 ± 10 meV
C (DIAMOND)	12.07 ± 0.03 amu	-45 ± 9 meV

References

- 1 P. C. Hohenberg and P. M. Platzmann, *Phys Rev* **152**, 198 (1966)
- 2 P. M. Platzmann in 'Momentum Distributions', ed R. N. Silver and P. E. Sokol (Plenum Press, New York, 1989, p249)
- 3 I Sick in ref 2, page 175.
- 4 R Newton, 'Scattering Theory of Waves and Particles', (Springer, Berlin, 1981)
- 5 V. F. Sears *Phys. Rev. B* **30**, 44 (1984)
- 6 J. Mayers *Phys. Rev. B* **41**, 41 (1991)
- 7 R. S. Holt, J. Mayers and A. D. Taylor (ref 2, p295)
- 8 R. A. Cowley and A. D. B. Woods, *Phys. Rev. Lett.* **21**, 787 (1968)
- 9 O. K. Harling, *Phys. Rev. Lett.* **24**, 1046 (1970)
- 10 H. A. Mook, *Phys. Rev. Lett.* **32**, 1167 (1974)
- 11 H. A. Mook, *Phys. Rev. Lett.* **51**, 1454 (1983)
- 12 P. Martel, E. C. Svensson, A. D. B. Woods, V. F. Sears and R. A. Cowley, *J. Low Temp. Phys.* **23**, 285 (1976)
- 13 W G Stirling, E F Talbot, B Tanatar and H R Glyde, *J Low Temp Phys* **73**, 33 (1988)
- 14 T. R. Sosnick, W. M. Snow, and P. E. Sokol, *Phys. Rev. B* **41**, 11185 (1990)
- 15 D. A. Peek, M. C. Schmidt, I. Fujita and R. O. Simmons, *Phys. Rev. B* **45**, 9671 (1992) and **45**, 9680 (1992)
- 16 H. Rauh and N. Watanabe, *Phys. Lett.* **100A**, 244 (1984)
- 17 R J Newport, P A Seeger and W G Williams, *Nuc Inst Meth* **A238** 177 (1985)
- 18 M. P. Paoli and R. S. Holt, *J. Phys. C* **21**, 3633 (1988)
- 19 S. Ikeda, K. Shibata, Y. Nakai and P. W. Stephens, *J. Phys. Soc. Japan* **61**, 2619 (1992)
- 20 B. Rosi-Schwartz, J. A. Blackmann, G. R. Mitchell and J. Mayers, *J. Phys. Condens. Matter* **4** 5665 (1992)
- 21 P J R Honeybone, R J Newport, W S Howells, J Tomkinson, S B Bennington and P J Revell, *Chem Phys Lett* **180** 145 (1991).
- 22 W S Howells, P J R Honeybone, R J Newport, S M Bennington and P J Revell. *Physica B* **180&181** 787, (1992).
- 23 P J R Honeybone, R J Newport, W S Howells and J Franks, Proc 'Diamond Films '91', Nice, September (1991)
- 24 J K Walters, P J R Honeybone D W Huxley, R J Newport and W S Howells, *J Phys Condens Matt*, Accepted for publication.
- 25 J Robertson, *Adv. Phys.* **35** 317 (1991)
- 26 J C Angus, P Koidl and S Domitz in 'Plasma Deposited Thin Films' edited by J Mort and F Jensen (CRC Press, Boca Raton, 1986).
- 27 D W Huxley, P J R Honeybone, R J Newport, W S Howells and J Franks. *Mat Res Soc Symp. Proc.* **170**, 493 (1992).
- 28 A. W Zou, K Reichelt, K Schmidt and B Dischler, *J Appl Phys* **65** 3914 (1989)
- 29 D R McKenzie, D Muller, B A Pailthorpe, Z H Wang, E Kravtchinskaja, D Segal, P B Lukins, P D Swift, P J Martin, G Amaratunga, P H Gaskell and A Saeed, *Diamond and Related Materials* **1** 51 (1991)

-
- 30 S W Lovesey 'Theory of Neutron Scattering from Condensed Matter', Oxford University Press, New York, (1987).
- 31 R N Silver Phys Rev B **37** 3794 (1988), **38** 2283 (1988), **39** 4022 (1989) and references therein.
- 32 G B West, in 'Momentum Distributions', (Ref 10) page 95.
- 33 M Warner , S W Lovesey and J Smith Z Phys B **51** 109 (1983)
- 34 J M F Gunn and M Warner Z Phys B **56** 13 (1984)
- 35 J Mayers, C Andreani and G Baciocco Phys Rev B **39** 2022 (1989)
- 36 P A Seeger, A D Taylor and R M Brugger Nuc Inst Meth **A240** 98 (1985)
- 37 C G Windsor 'Pulsed Neutron Scattering', Taylor and Francis (1981)
- 38 J. Mayers and A. C. Evans, Rutherford Appleton Laboratory Report RAL-91-048 (1991)
- 39 J Mayers, A C Evans to be published
- 40 C Andreani, G Baciocco, R S Holt and J Mayers Nuc Inst Meth **A276** 297 (1989)
- 41 J Franks, Vacuum **34** 259 (1984)
- 42 A. Dehbi-Alaoui, A Matthews and J Franks. Surface and Coatings Technol. **47** 722 (1991)
- 43 S Stringari, Phys Rev B **35** 2038 (1987)
- 44 J. K. Walter, P. J. R. Honeybone, D W Huxley, R J Newport and W S Howells to be published.
- 45 J. A. Young and J. U. Koppel, J. Chem. Phys. **42**, 357 (1965)
- 46 D. F. McMorrow, R.A. Cowley, R. M. Nicklow, P.W. Mitchell , A. D. Taylor and M. Mostoller, J. Phys. C, **2**, 1045 (1990)
- 47 J Mayers Rutherford Appleton Laboratory Report, RAL-93-041 (1993)

Figure Captions

Figure 1. Schematic diagram of inverse geometry time of flight spectrometer.

Figure 2. The eVS instrument

Figure 3. Neutron time of flight spectra obtained from a-C:H at the 10 different scattering angles available on the forward scattering detectors of eVS. The angle increases in steps of 2° from the lowest scattering angle of 36° at the bottom to the highest scattering angle of 54° at the top. The right hand peak is caused by scattering from carbon while the left hand peak is due to hydrogen scattering.

Figure 4. . Compton profile $J_M^a(y_M)$ for H in a-C:H, obtained by combining all forward angle data sets as described in equation 14. The solid line is the fit described in the text, the dotted line is the instrument resolution function.

Figure 5. Values of σ_M^θ and σ_{MS}^θ derived from fits to data sets obtained at different scattering angles. Within statistical error no systematic variation with scattering angle is observed. The mean values of $\bar{\sigma}_M^\theta$ (solid line) and $\bar{\sigma}_{MS}^\theta$ (dashed line) are also shown.

Figure 6. Sum of 30 time of flight spectra collected from a-C:H. The three peaks correspond to detection at the three U resonances used for measurement. The expected positions of peaks from C (+) and Al (*) are indicated.

Figure 7. Compton profile $J_M^a(y_M)$ for carbon obtained from the diamond sample by using the 6671 meV U resonance as described in the text. The solid line is the fit, the dotted line the resolution function.

Figure 8. Experimental values of $\bar{\omega}_M$ as a function \bar{q}_M^2 for the H atom in a-C-H. The solid line is a fit to equation 15.

Figure 9. The quantity $\varepsilon = \bar{\omega}_M - \bar{q}_M^2 / 2M$ as a function of \bar{q}_M^2 for hydrogen in a-C:H. The mean value of -54 ± 6 meV is also shown as a solid line.

Figure 10. Experimental values of $\bar{\omega}_M$ as a function \bar{q}_M^2 for the C atom in a-C-H. . The solid line is a fit to equation 15. The three clusters of points correspond to measurements using the three U resonances.

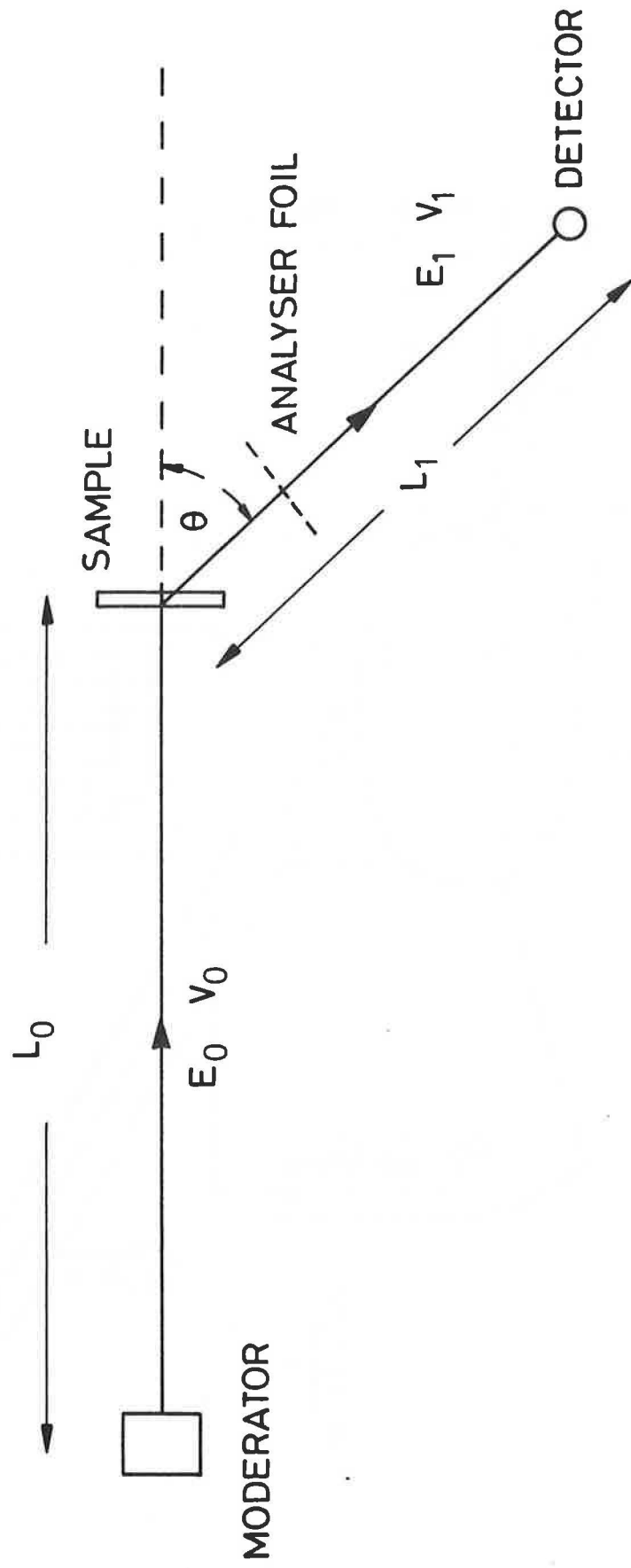


Figure 1

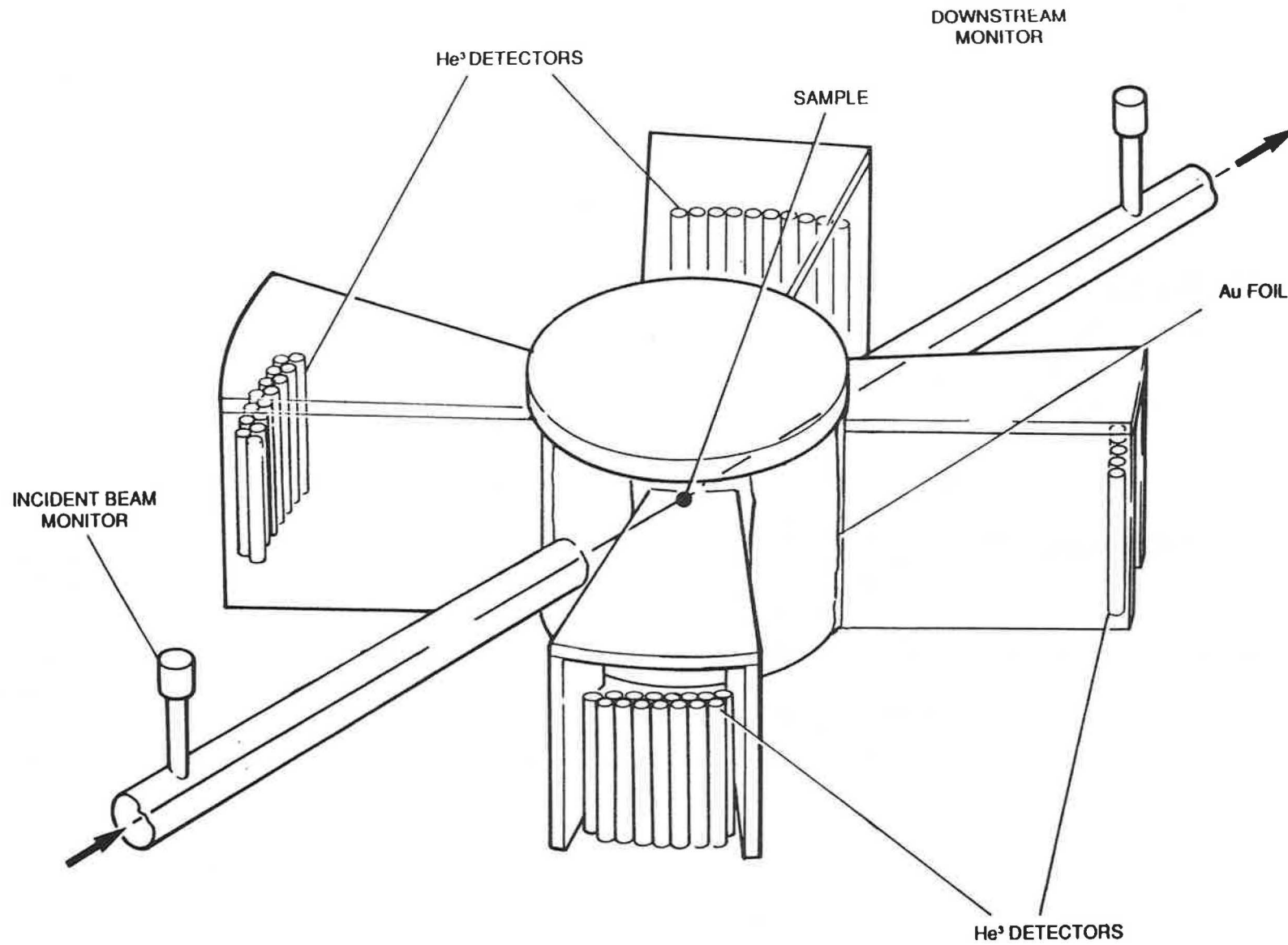


Figure 2 THE eVS SPECTROMETER

Figure 3

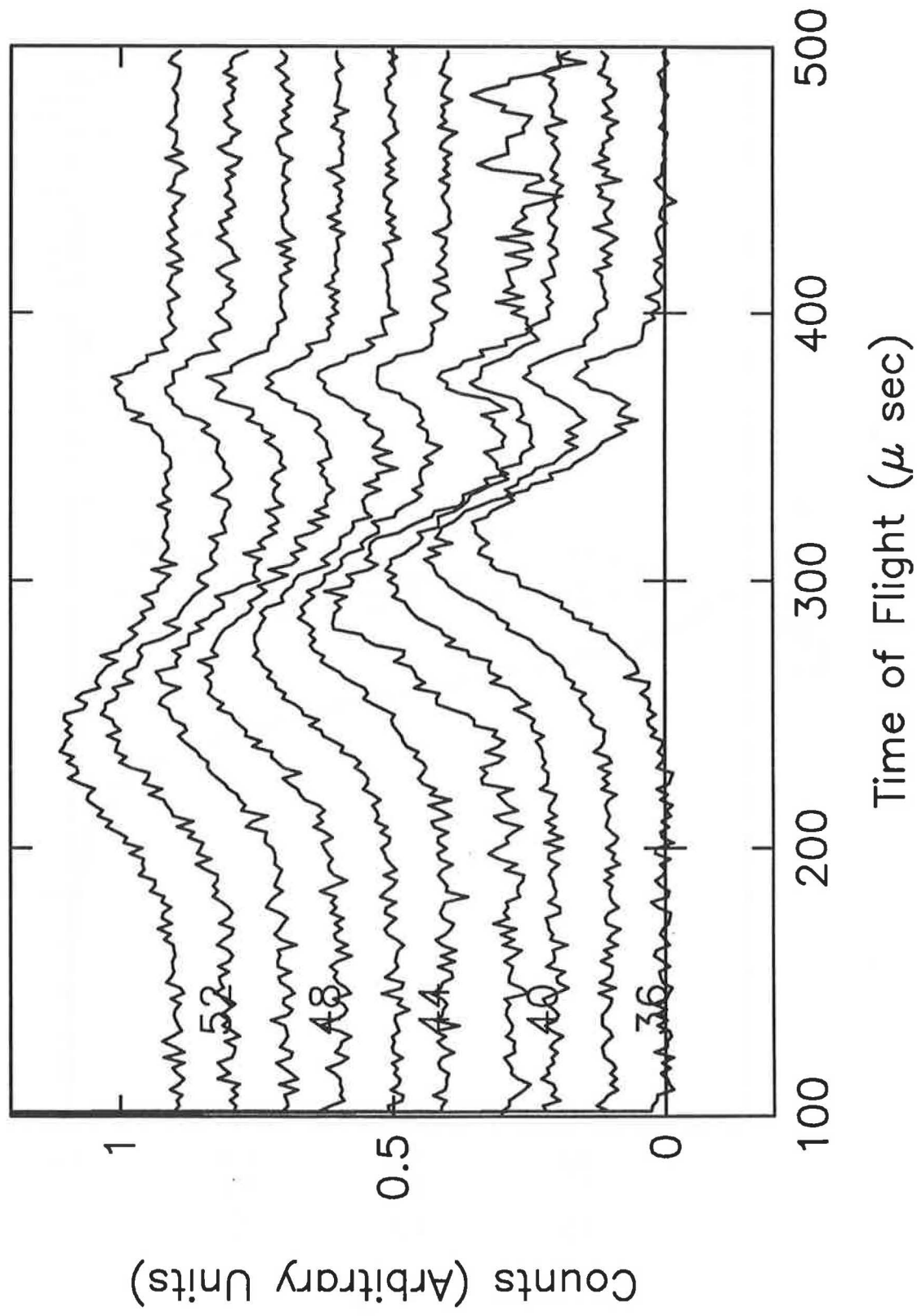


Figure 4

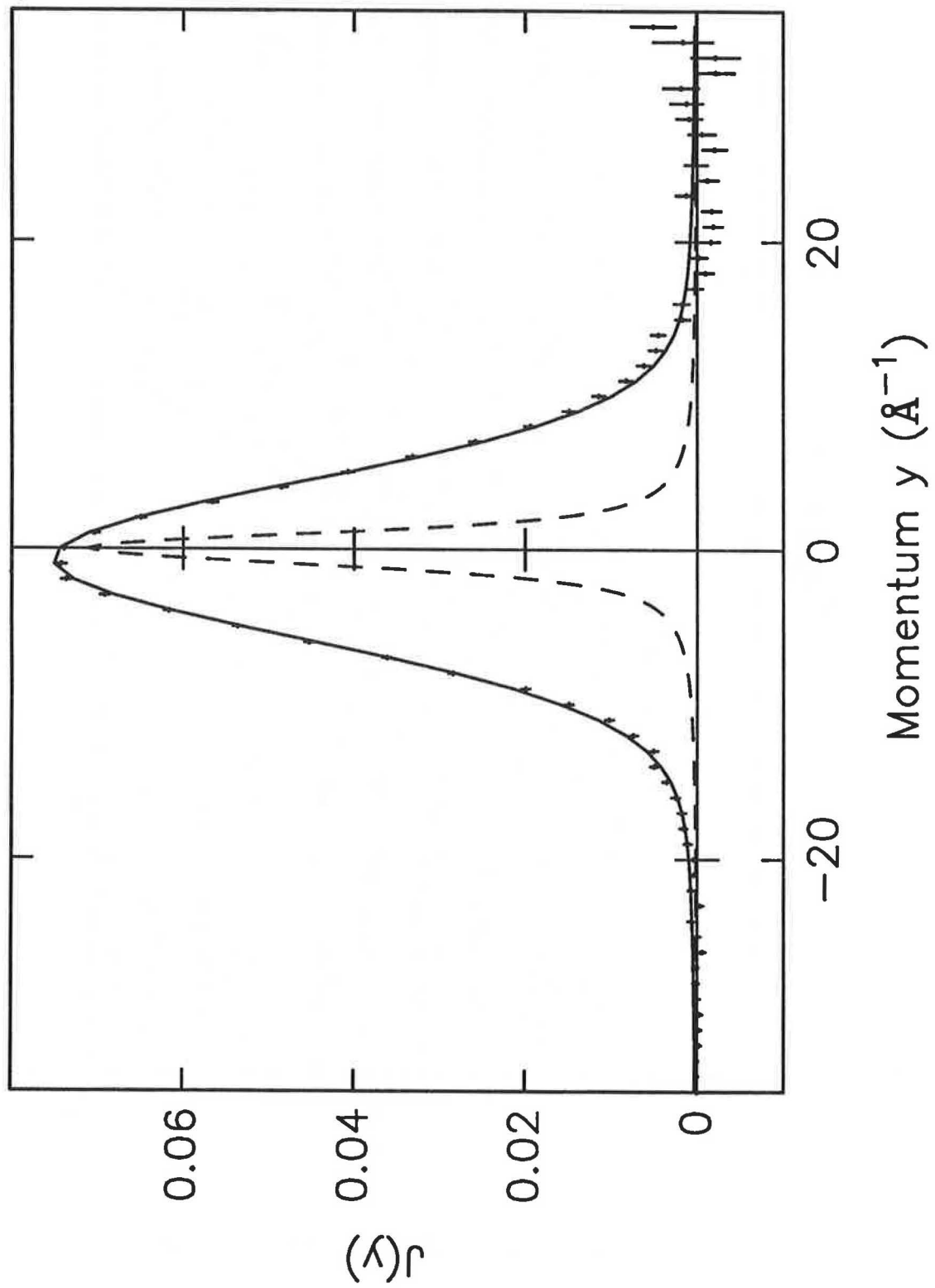


FIGURE 5

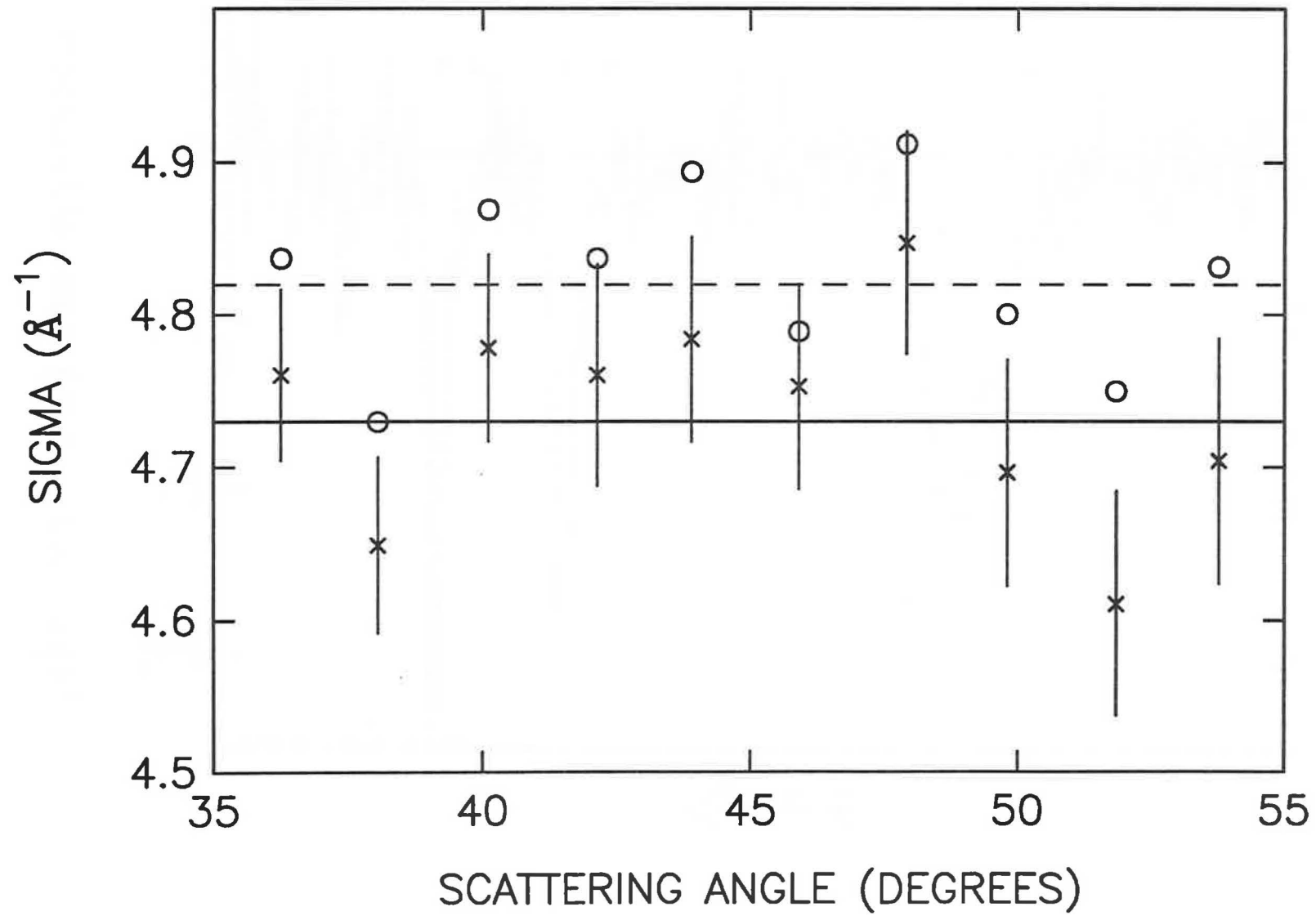


Figure 6

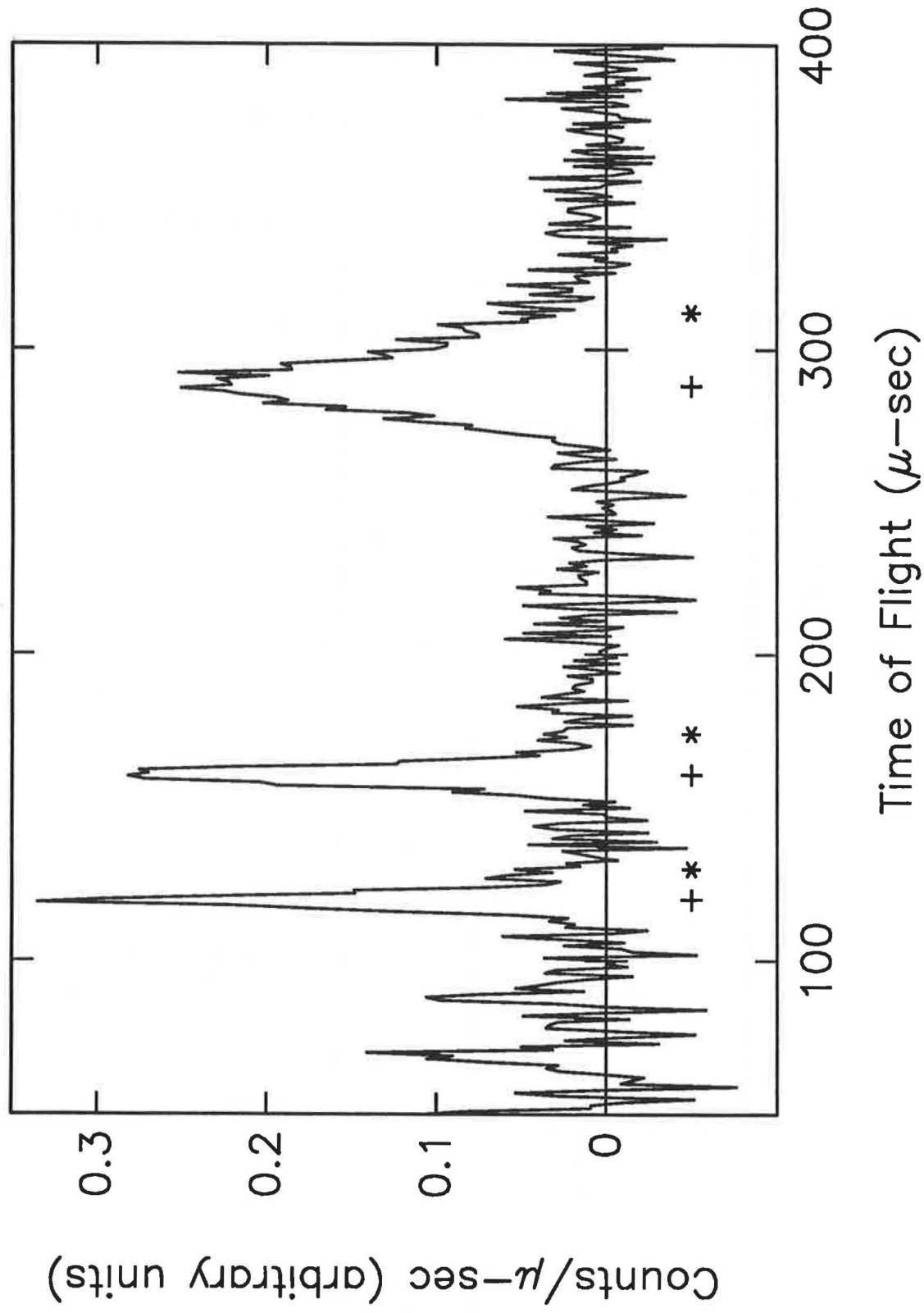


Figure 7

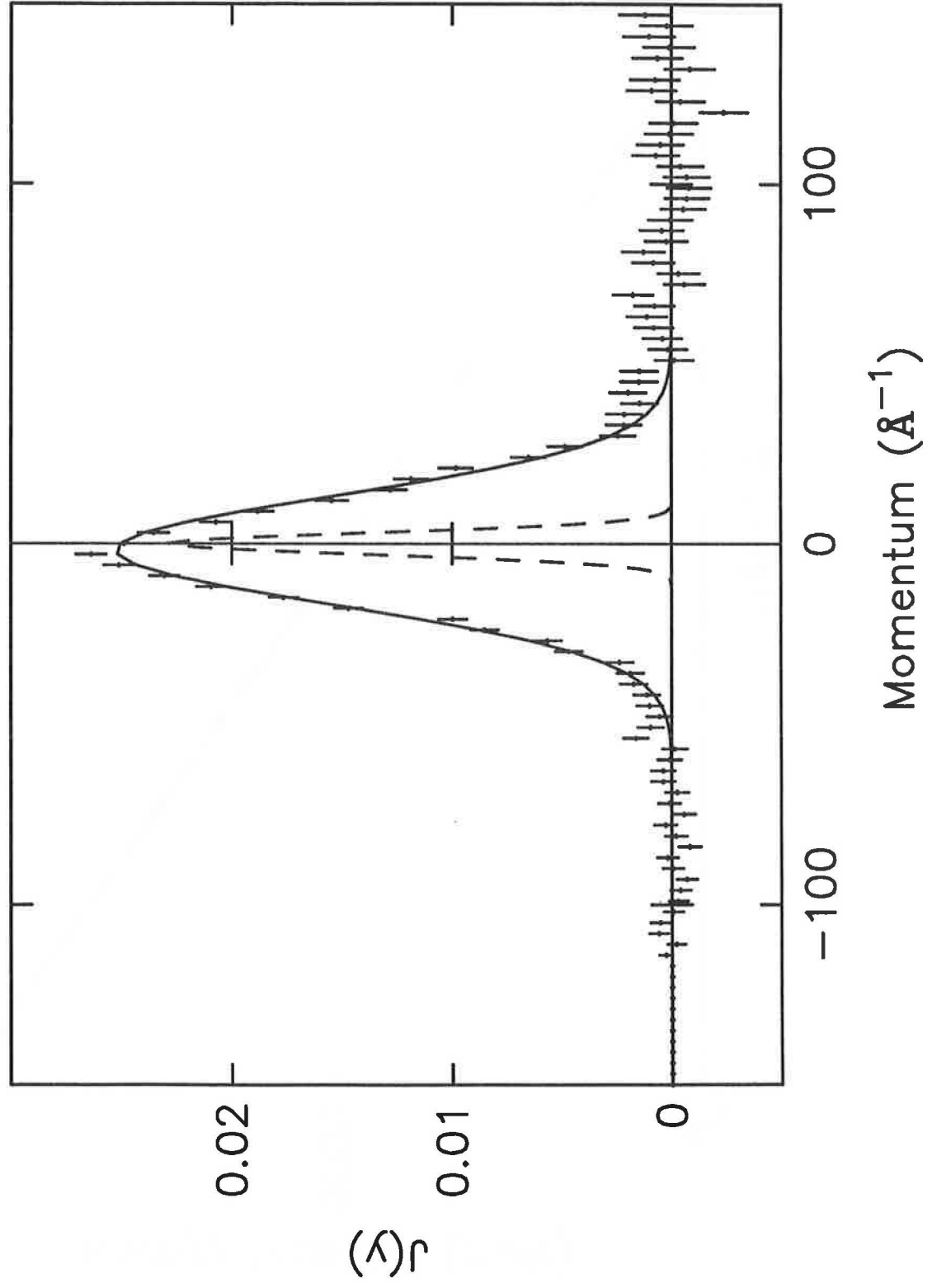


Figure 8

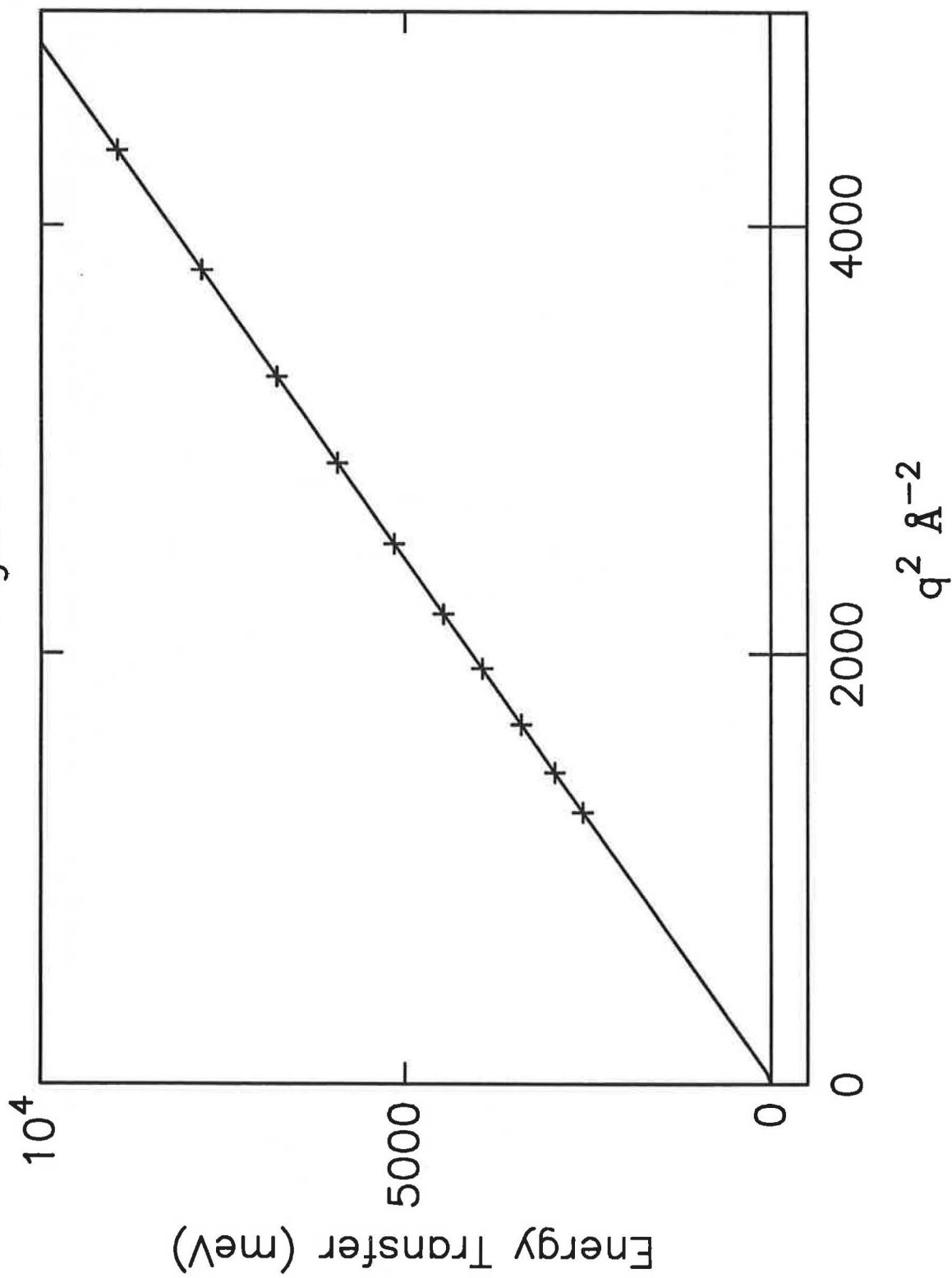


Figure 9

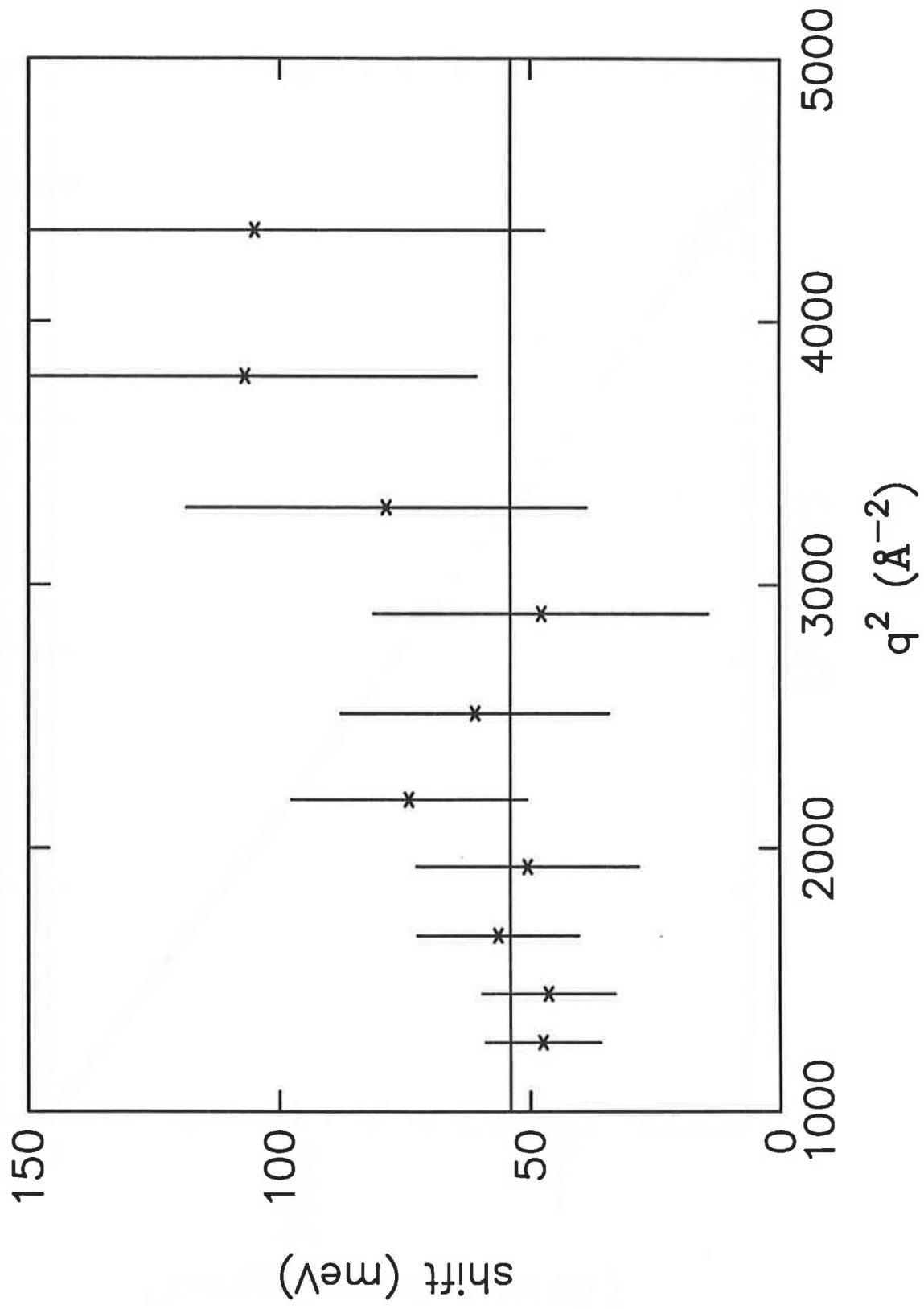


Figure 10

